Anisotropic Seismic Imaging and Inversion for Subsurface Characterization at the Blue Mountain Geothermal Field in Nevada

Lianjie Huang[1], Kai Gao[1], Yunsong Huang[1], and Trenton T. Cladouhos[2]

[1]Geophysics Group, Los Alamos National Laboratory, Los Alamos, NM 87545, USA

[2]AltaRock Energy, Inc., Seattle, WA 98103, USA

ljh@lanl.gov; kaigao@lanl.gov; yunsongh@lanl.gov; tcladouhos@altarockenergy.com

Keywords: Anisotropy, anisotropic elastic-waveform inversion, anisotropic reverse-time migration, Blue Mountain, fault, fracture zone, full-waveform inversion, geothermal.

ABSTRACT

The Blue Mountain geothermal power plant is located at the base of Blue Mountain, west of Winnemucca, Nevada. The power plant was built in 2009 with an installed gross capacity of 49.5 MW and net capacity of 39.5 MW. Currently, the net power production is 29 MW because production temperatures declined steeply for the first 4 years of production but was mitigated recently. Now, the project owner, AltaRock Energy is implementing an improvement plan to increase the production to plant capacity. Subsurface characterization is crucial for new well placement. In 2007, seismic data along seven 2D lines were acquired at Blue Mountain for subsurface characterization. The data contain strong ground-roll noise, resulting in a great challenge for full-waveform-based anisotropic inversion and migration imaging. We employ our newly developed wavenumber-adaptive frequency-space filtering technique to successfully remove the ground-roll noise and obtain high-quality pre-stack seismic waveform data for seismic-waveform inversion and reverse-time imaging. We build anisotropic models along the seven 2D lines using anisotropic elastic-waveform inversion of the processed seismic data. We then conduct anisotropic reverse-time migration using the anisotropic models and our newly processed seismic data to obtain high-resolution subsurface images at Blue Mountain The high-resolution subsurface images reveal many geologic structures/faults that are invisible on the previous industry Kirchhoff migration images. The new seismic images can provide valuable information for design and selection of future geophysical studies to further characterize these features and eventually for optimizing the placement of new wells.

1. INTRODUCTION

The Blue Mountain geothermal field (Figure 1), located in the Basin and Range of northern Nevada, has been in operation since November 2009. The power plant was designed to generate 49.5 MW of gross capacity and 39.5MW of net capacity. From 2009 to 2013, the resource experienced significant temperature decline because of reinjection into wells on the west side of the field, down-dip of the production zone. Since 2013, all but one of the western injectors have been idle, with reinjection moved to the northern and northeastern edges of the field. Wells on the southern edge of the field, where new reinjection could mine significant stranded heat-in-place, remain idle because of low permeability. Former injection wells at the western edge of the field were initially very hot but they may not re-heat to pre-injection temperatures. Thus, new, hot production wells at the western edge of the field may be needed to bring the plant production back up to initial production.

(a) Blue Mountain geothermal field   (b) Geothermal power plant (AltaRock, 2013)

Figure 1: Blue mountain geothermal field and the geothermal power plant.

The fracture zones and faults intersect with active production and injection wells according to the results of tracer tests and eight years of experience of shifting injection and production to maximize total flow rate and temperatures to the plant (Swyer, et al., 2016). However, away from the active geothermal field, in step-out regions, the permeability is less well-characterized. Therefore, the field operator,

AltaRock Energy, has contributed passive seismic data, active seismic data, and geophysical surveys to the project in order to better map fracture permeability in the field. This information will inform future decisions about which wells to hydraulically stimulate and, if necessary, where to site potential new injectors or producers.

In 2007, Optim, Inc. carried out an active seismic survey along seven 2D lines at the Blue Mountain geothermal field for subsurface characterization (Optim, 2007). Optim built a tomography velocity model using first-arrival traveltimes and conducted prestack Kirchhoff depth migration for each line of seismic data. Kirchhoff migration is based on ray tracing (e.g. Keho and Beydoun, 1988; Gray and May, 1994).

During the last decade or so, full-waveform inversion (FWI) (Tarantola, 1984) has become a powerful tool to build high-resolution subsurface velocity models for subsurface characterization and improving migration imaging (e.g. Lin and Huang, 2014, 2017; Chi et al., 2017). FWI inverts seismic waveforms for a subsurface velocity model by matching synthetic seismic waveforms (instead of first-arrival traveltimes) with real seismic waveforms. In addition, reverse-time migration (RTM) (Chang and McMechan, 1986, 1987) has also been developed as an arguably the most effective migration technique for high-resolution imaging of subsurface complex structures (e.g. Tan and Huang, 2014; Chen and Huang, 2015; Gao et al. 2017). Both FWI and RTM are based on wave theory instead of ray theory for seismic inversion and imaging.

Making use of the entire waveform for seismic inversion and imaging is particularly important for imaging fracture zones and complex structures within geothermal reservoirs because of complicated seismic-wave scattering from fracture zones. The seismic data acquired by Optim at the Blue Mountain geothermal field contain high-level of noise, in addition to strong ground-roll noise that has to be removed for seismic-waveform-based inversion and migration imaging.

We apply our newly developed wavenumber-adaptive bandpass filter (Huang, et al., 2017) to seismic data along seven 2D lines acquired at Blue Mountain to remove most of ground-roll noise. We use these data to conduct anisotropic elastic-waveform inversion (AEWI) to obtain subsurface velocity models and other anisotropic elastic parameters. Finally, we employ anisotropic reverse-time migration to obtain high-resolution subsurface images along seven 2D lines.

We first briefly describe the methodology, present results of anisotropic elastic-waveform inversion and anisotropic reverse-time migration of Blue Mountain seismic data along seven 2D lines, and compare imaging results with industry Kirchhoff migration images. Our anisotropic reverse-time migration yields clear subsurface images with significantly less image noise compared to the industry Kirchhoff migration images.

2. METHODOLOTY

To estimate anisotropic properties of subsurface media at the Blue Mountain geothermal field, we use anisotropic elastic-waveform inversion to invert for the P- and S-wave velocities, the density and the Thomsen parameters.

Anisotropic elastic-waveform inversion (AEWI) is based on the elastic-wave equation in the following first-order form:

$$\rho \frac{\partial \mathbf{v}}{\partial t} = \Lambda \sigma + \mathbf{f}, \tag{1}$$

$$\frac{\partial \sigma}{\partial t} = \mathbf{C} \Lambda^{\mathrm{T}} \mathbf{v}, \tag{2}$$

where $\mathbf{v} = (v_x, v_y)^{\mathrm{T}}$ is the particle velocity of wavefield, $\sigma = (\sigma_{xx}, \sigma_{zz}, \sigma_{xz})^{\mathrm{T}}$ is the stress wavefield, Λ is a differential operator (Vigh et al., 2014), ρ is the density, and $\mathbf{C} = (C_{ij})$ is the elasticity matrix.

AEWI is to invert for subsurface anisotropic properties by minimizing the following misfit function between synthetic seismic-waveform data $f(\mathbf{m})$ and field seismic-waveform data $\mathbf{d}$:

$$\chi(\mathbf{m}) = \sum_{N_s, N_r} \int_0^T [\mathbf{d} - f(\mathbf{m})]^2 \, dt, \tag{3}$$

where N_s and N_r represent the number of sources and receivers, respectively, and $\mathbf{m}$ is anisotropic elastic parameters. For field data applications, matching seismic waveform amplitudes using equation (3) could be very challenging and the inversion could converge to a local minimum of the misfit function. This challenge can be even more severe considering the fact that our AWEI algorithm is based on elastic theory without attenuation, but seismic waves attenuate during propagation through subsurface media. In addition, the source and receiver couplings are usually far from perfect when recording land seismic data. Therefore, we employ the following correlation-type misfit function (Chi et al., 2015) to alleviate such difficulty:

$$\chi(\mathbf{m}) = \sum_{N_s,N_r}\left[1 - \frac{\int df(\mathbf{m})\,dt}{\int f(\mathbf{m})\,f(\mathbf{m})\,dt}\right].$$ (4)

We invert for the P- and S-wave velocity and Thomsen parameters (Thomsen, 1986) of subsurface media that have more clear physical meanings compared with the elasticity parameters $C_{ij}(i,j=1,2,...,6)$. We compute the gradients of the misfit function with respect to the velocities, the density and Thomsen parameters using the chain rule of differentiation:

$$\frac{\partial \chi}{\partial m} = \sum_{i,j}\frac{\partial \chi}{\partial C_{ij}}\frac{\partial C_{ij}}{\partial m},$$ (5)

where $m = V_p$, V_s, ε or δ, and the gradients of the misfit function w.r.t. the elasticity parameters can be relatively easily computed (Vigh et al., 2014).

We employ the limited-memory Broyden-Fletcher-Goldfarb-Shanno (BFGS) inversion framework and a wavefield energy preconditioning strategy to accelerate the convergence of AWEI. In addition, we use different step lengths for different inversion parameters during the optimal step size search.

After building an anisotropic elastic model using our AWEI, we perform anisotropic reverse-time migration (ARTM) to produce subsurface structural images. We use the following wavefield-separation-based RTM imaging condition (Fei et al., 2015; Gao et al., 2017) to reduce image artifacts and improve image resolution:

$$I = \sum_{N_s,N_r}\int_0^T\left[u_s u_r - H_z(u_s)H_z(u_r) - u_s H_t(H_t(u_r)) - H_z(u_s)H_t(u_r)\right]dt,$$ (6)

where H_z and H_t represent the Hilbert transform in the vertical and temporal directions, respectively, and u_s and u_r represents the source and receiver wavefields, respectively.

3. RESULTS

The Blue Mountain geothermal resource is located at a structural complication. The subsurface geology at the Blue Mountain field was characterized using data from 20 deep wells (AltaRock, 2013; Swyer et al., 2016). Figure 2 is AltaRock's conceptual fault model for fluid flow based on geophysical data, well lithology logs, well temperature logs, and tracer data. Within the geothermal field, the locations of the faults are consistent with gravity inversion and microseismic event locations.

Optim, Inc. acquired seismic data along seven 2D lines as shown in Figure 3 at the Blue Mountain geothermal field in 2007. The lengths of the seven 2D seismic lines vary from approximately 4 km to 6 km. The regions with higher elevations at the eastern end of the seven lines are along the toe of Blue Mountain shown in Figure 2. Stationary receivers were placed along each line to record seismic data for active sources at different positions along the line. The receiver elevation varies from approximately 1250 m to 1600 m. For all the seven seismic survey lines, the receiver interval is approximately 33.5 m, and the source point interval is approximately 67 m. Dynamite sources were used for acquiring seismic data, and the seismic data contain only one vertical component. We use this component of data as the vertical displacement component to conduct anisotropic elastic-waveform inversion.

Figure 4(a) shows that the industry processed seismic data acquired at Blue Mountain still contain significant strong ground-roll noise (or surface waves). We apply our recently developed wavenumber-adaptive bandpass filter (Huang, et al., 2017) to the industry-processed seismic data to reduce strong ground-roll noise, as shown in Figure 4(b). We use these data for our anisotropic elastic-waveform inversion and anisotropic reverse-time migration.

AEWI requires appropriate initial models of anisotropic elastic parameters to obtain reliable inversion results. The only available parameter models for the Blue Mountain data are a set of smooth P-wave velocity models obtained using traveltime tomography of first arrivals in seismic data. These velocity models have the maximum effective depth of approximately 1 km below surface. For our seismic inversion and imaging using seismic reflection data, we simply extrapolate the velocity models to the deeper regions using the bottom layer's velocity values as the initial models for full-waveform inversion (Figure 5a).

We build the initial S-wave velocity models by scaling the initial P-wave velocity model with a factor of 0.58 (approximately the inverse of 1.732) (Figure 5b). We construct the initial density models from the initial P-wave velocity models using Gardner's equation $\rho = 0.31V_p^{0.25}$. We generate the initial Thomsen parameters by setting the near-surface region to be transversely isotropic with vertical symmetry axis (VTI) while the deeper regions to be transversely isotropic with horizontal symmetry axis (HTI). Figure 5 shows the initial models (P- and S-wave velocities and Thomsen parameters ε and δ) of Line 1 as an example. We built the initial models for all seven 2D lines in the same approach for anisotropic elastic-waveform inversion.

Huang et al.

We conduct anisotropic elastic-waveform inversion of LANL's filtered seismic data for all seven 2D lines from Blue Mountain, and obtain updated models anisotropic elastic parameters. Figure 6 displays our inversion results of P- and S-wave velocities and Thomsen parameters ε and δ) for Line 1 as an example of our anisotropic elastic-waveform inversions.
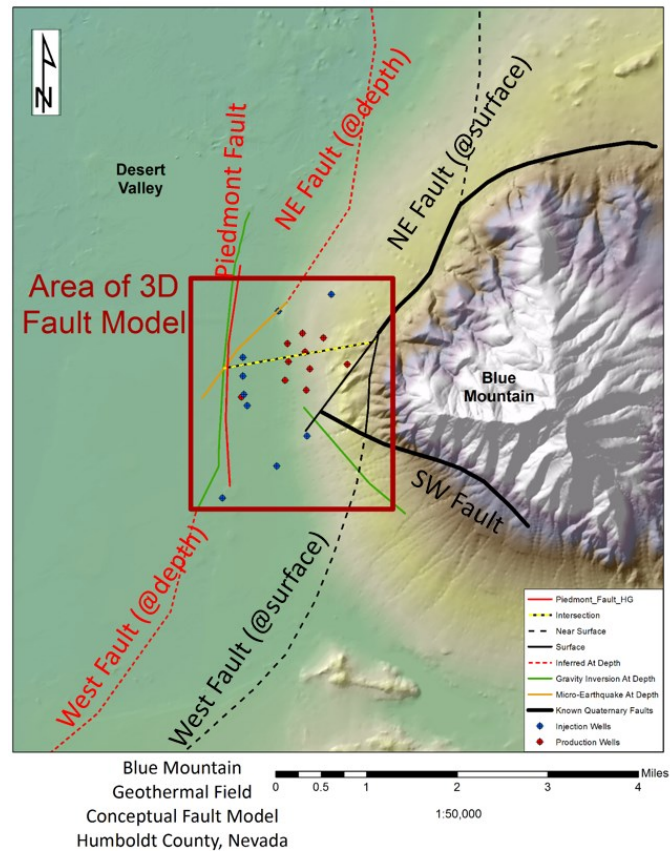

Figure 2: Conceptual fault model of the Blue Mountain geothermal field inferred from gravity inversion and microseismicity (AltaRock, 2013, Swyer et al., 2016).
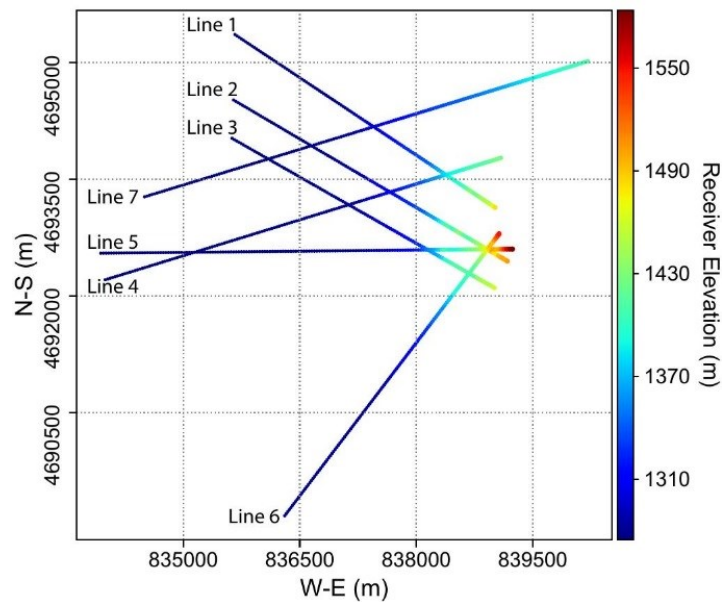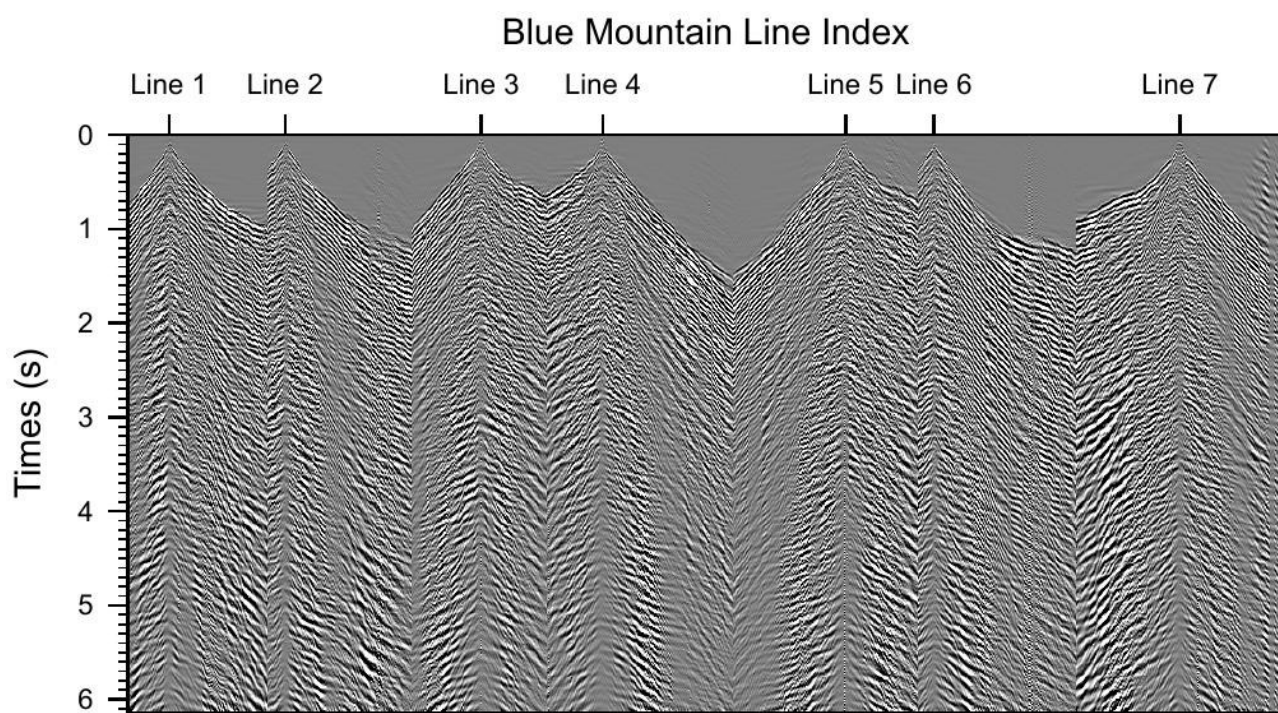

Figure 3: Seven 2D lines for acquiring active seismic reflection data at the Blue Mountain geothermal field.

Blue Mountain Line Index
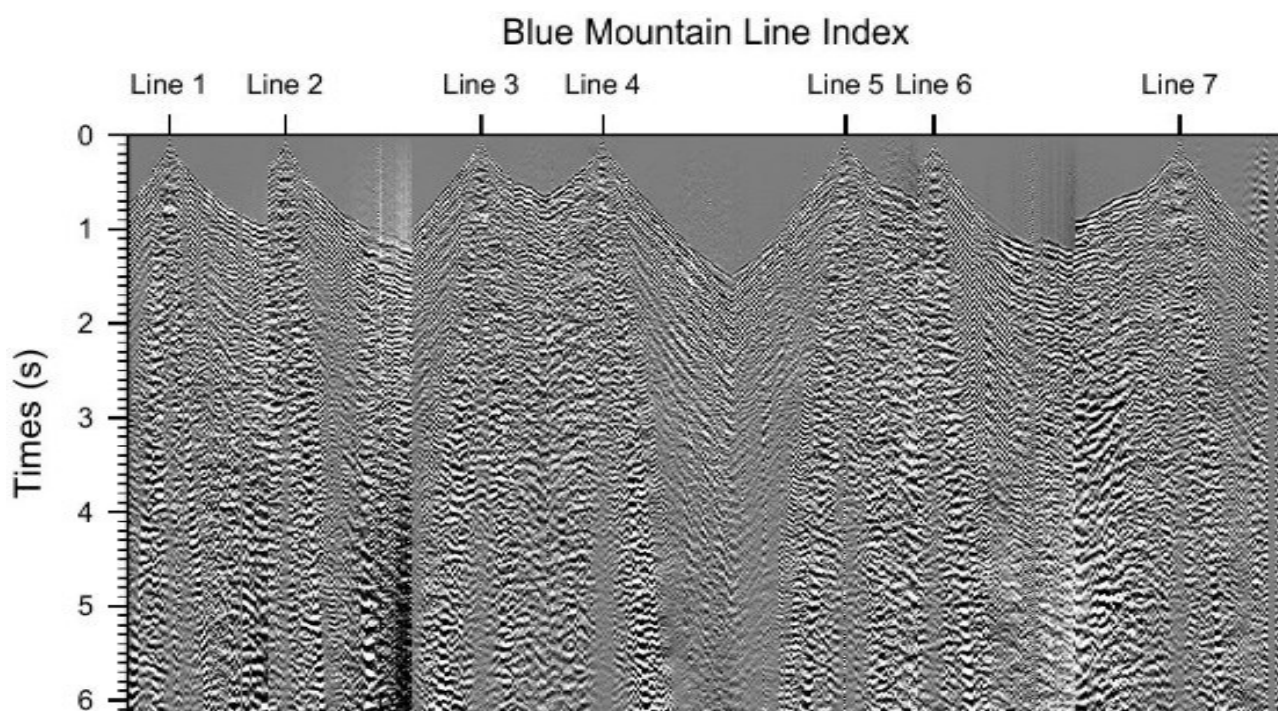
(a) Industry processed example Blue Mountain seismic data.

Blue Mountain Line Index

(b) Example Blue Mountain seismic data after applying LANL's wavenumber-adaptive bandpass filter to seismic data in (a).

Figure 4: (a) Industry processed seismic data acquired at Blue Mountain still contain strong ground-roll and other noises; (b) The strong ground-roll noise are significantly reduced after applying LANL's novel wavenumber-adaptive bandpass filter to industry-processed data.
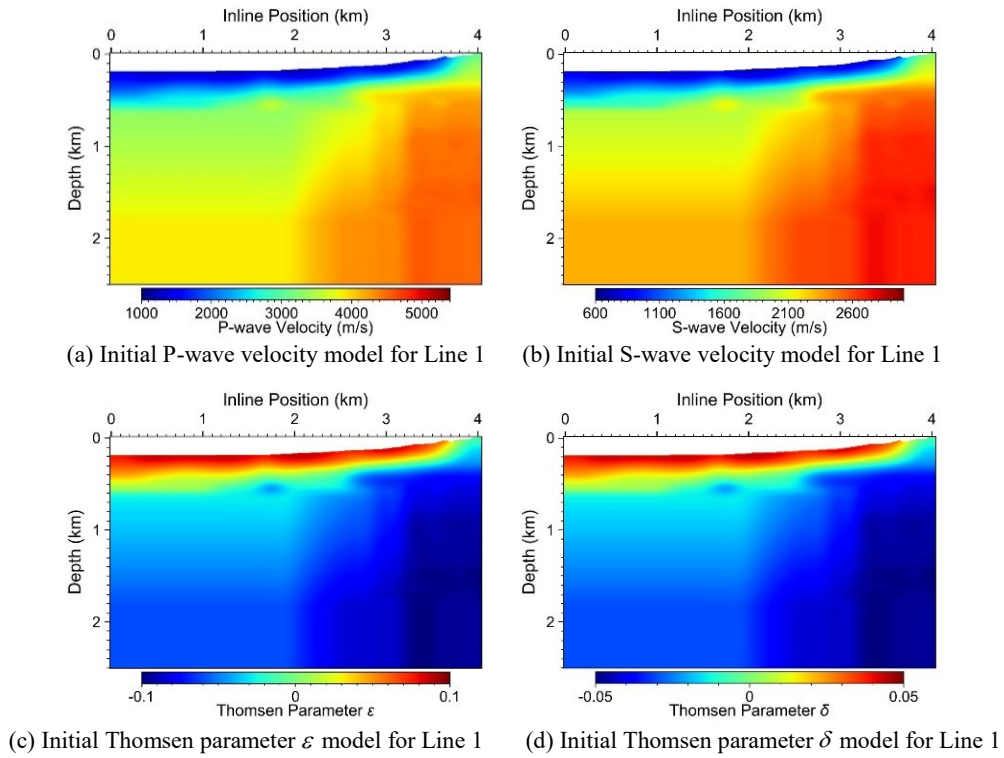
(a) Initial P-wave velocity model for Line 1   (b) Initial S-wave velocity model for Line 1

(c) Initial Thomsen parameter ε model for Line 1   (d) Initial Thomsen parameter δ model for Line 1

Figure 5: Initial P- and S-wave velocity models (a-b) and initial Thomsen parameters ε and δ models (c-d) of Line 1 for anisotropic elastic-waveform inversion.
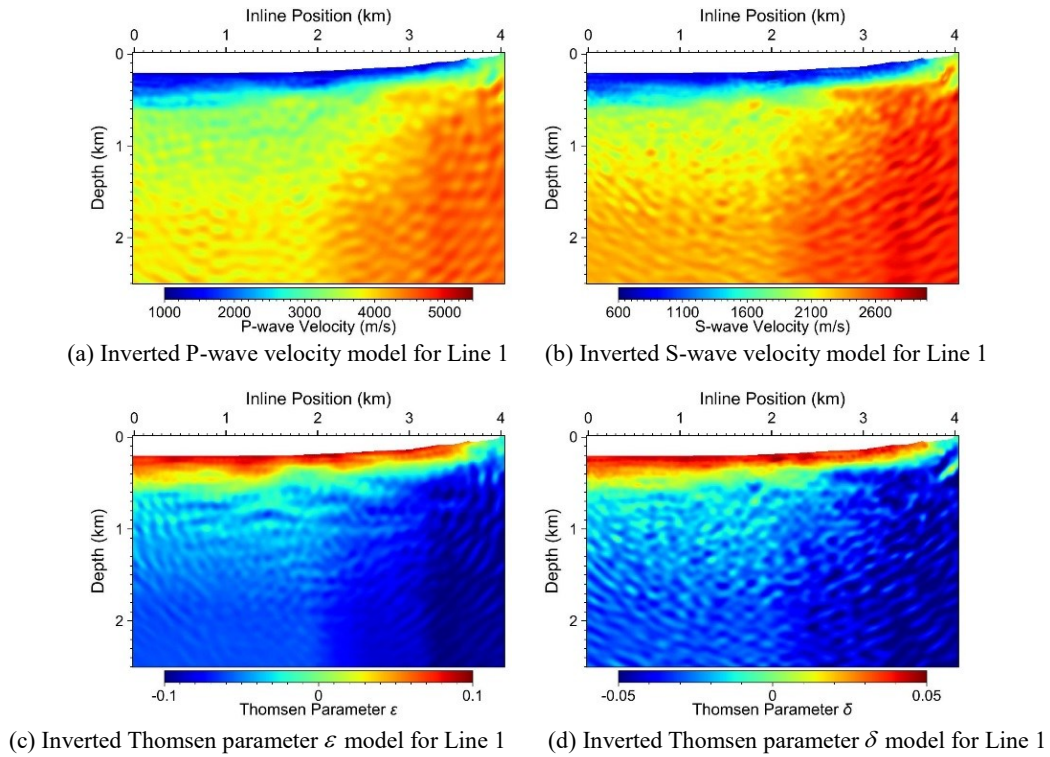

(a) Inverted P-wave velocity model for Line 1   (b) Inverted S-wave velocity model for Line 1

(c) Inverted Thomsen parameter ε model for Line 1   (d) Inverted Thomsen parameter δ model for Line 1

Figure 6: Inverted P- and S-wave velocity models (a-b) and Thomsen parameters ε and δ models (c-d) of Line 1 obtained using anisotropic elastic-waveform inversion.
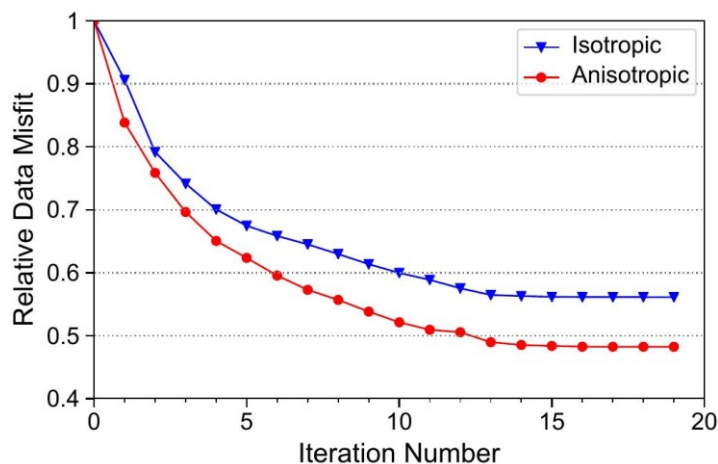
Figure 7: Comparison between the convergence rate of anisotropic elastic-waveform inversion and that of isotropic elastic-waveform inversion for seismic data of Line 1 acquired at the Blue Mountain geothermal field, showing that anisotropic elastic-waveform inversion further reduces approximately 10% of relative data misfit compared to that for isotropic elastic-waveform inversion.

Figure 7 is a comparison between the convergence rate of anisotropic elastic-waveform inversion and that of isotropic elastic-waveform inversion for seismic data along Line 1. Isotropic elastic-waveform inversion inverts for only the P- and S-wave velocities and the density, while anisotropic elastic-waveform inversion inverts for Thomsen anisotropic parameters in addition to these three elastic parameters. Figure 7 shows that anisotropic elastic-waveform inversion reduces additional approximately 10% of relative data misfit compared to that for isotropic elastic-waveform inversion. This data misfit reduction indicates that it is necessary to consider the subsurface as anisotropic media for seismic inversion and imaging.

The additional data misfit reductions of anisotropic elastic-waveform inversion vs isotropic elastic-waveform inversion for seismic data along Lines 2, 4, and 7 are similar to that for seismic data along Line 1. This additional data misfit reduction for seismic data along Lines 3, 5, and 6 are not significant. Nevertheless, anisotropic elastic-waveform inversion of seismic data from Blue Mountain mostly converts better than isotropic elastic-waveform inversion.

After we obtain updated anisotropic elastic parameters from anisotropic elastic-waveform inversion of all seismic data from Blue Mountain, we conduct anisotropic reverse-time migration of the data to obtain images of subsurface structures. We also compare our results with industry-generated Kirchhoff migration images. Figure 8-Figure 14 shows the comparisons of our new migration images with the Kirchhoff migration images for seismic data of Lines 1 to 7, respectively.

Kirchhoff migration produces noisy images, and cannot image regions deeper than approximately 1.5 km. By contrast, our anisotropic RTM yields subsurface images with significantly less image noise, and provides clear images from shallow to deep regions (up to 2.5 km in our current implementation).
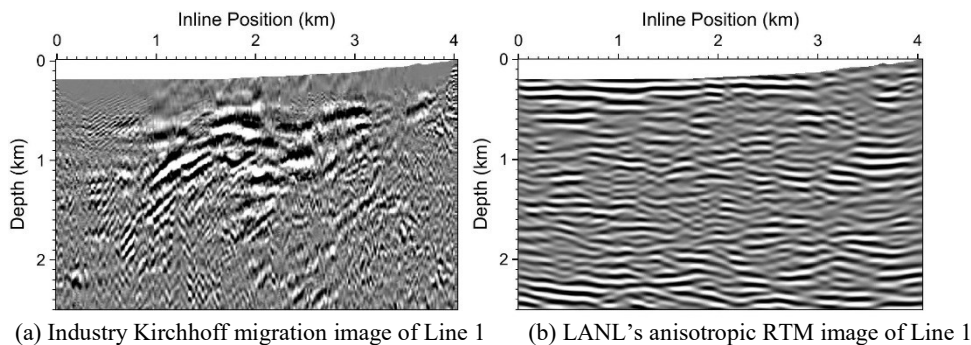

(a) Industry Kirchhoff migration image of Line 1 (b) LANL's anisotropic RTM image of Line 1

Figure 8: Line 1 image comparison between industry Kirchhoff migration image (a) and LANL's anisotropic reverse-time migration image (b).
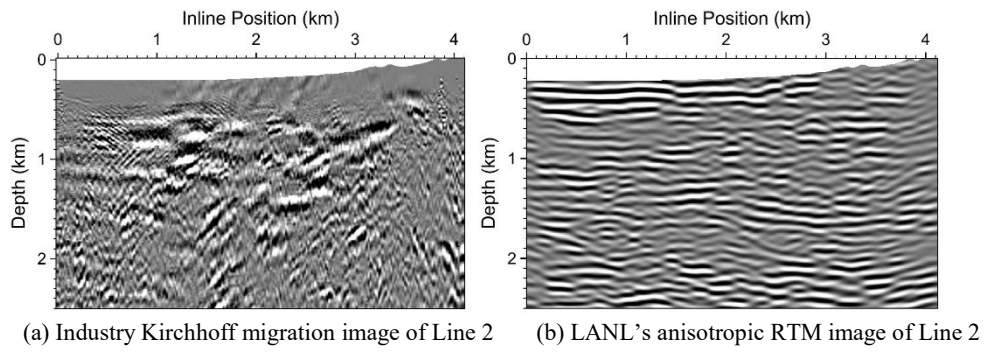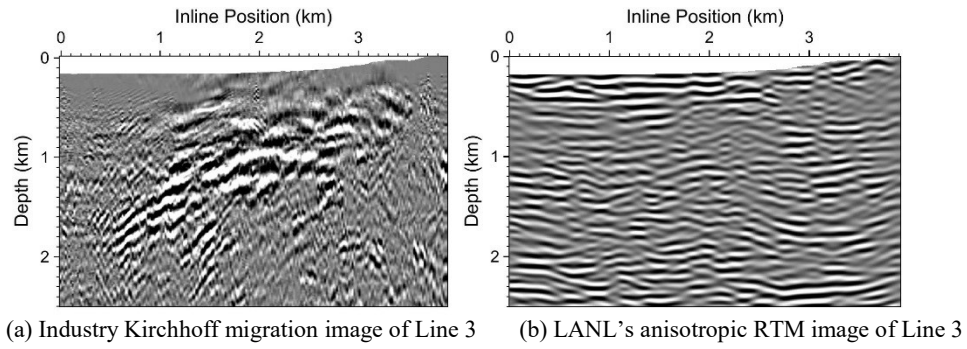
(a) Industry Kirchhoff migration image of Line 2   (b) LANL's anisotropic RTM image of Line 2

Figure 9: Line 2 image comparison between industry Kirchhoff migration image (a) and LANL's anisotropic reverse-time migration image (b).
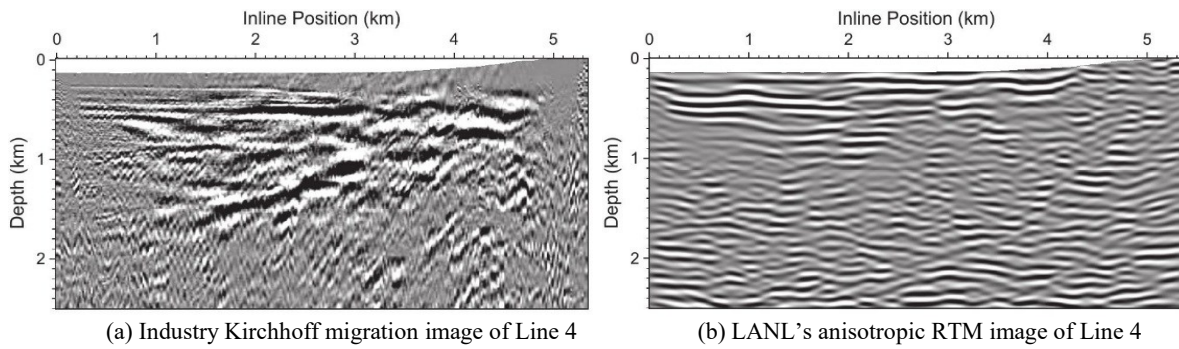

(a) Industry Kirchhoff migration image of Line 3   (b) LANL's anisotropic RTM image of Line 3

Figure 10: Line 3 image comparison between industry Kirchhoff migration image (a) and LANL's anisotropic reverse-time migration image (b).
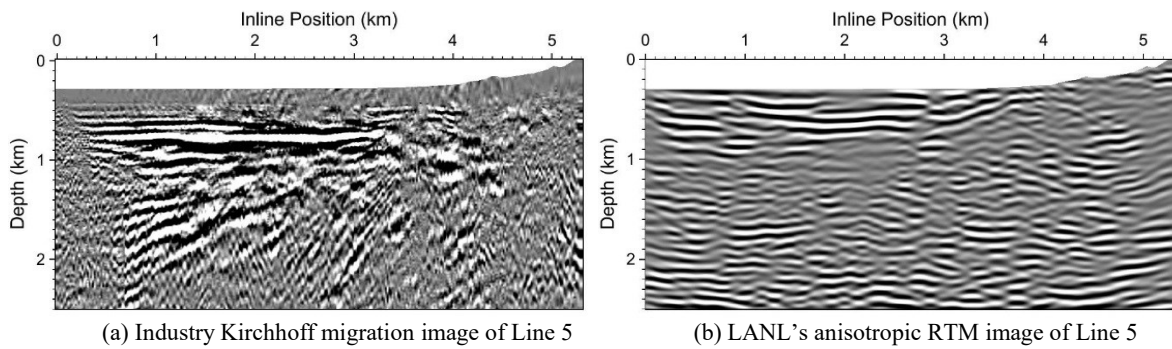

(a) Industry Kirchhoff migration image of Line 4   (b) LANL's anisotropic RTM image of Line 4

Figure 11: Line 4 image comparison between industry Kirchhoff migration image (a) and LANL's anisotropic reverse-time migration image (b).

(a) Industry Kirchhoff migration image of Line 5   (b) LANL's anisotropic RTM image of Line 5

Figure 12: Line 5 image comparison between industry Kirchhoff migration image (a) and LANL's anisotropic reverse-time migration image (b).
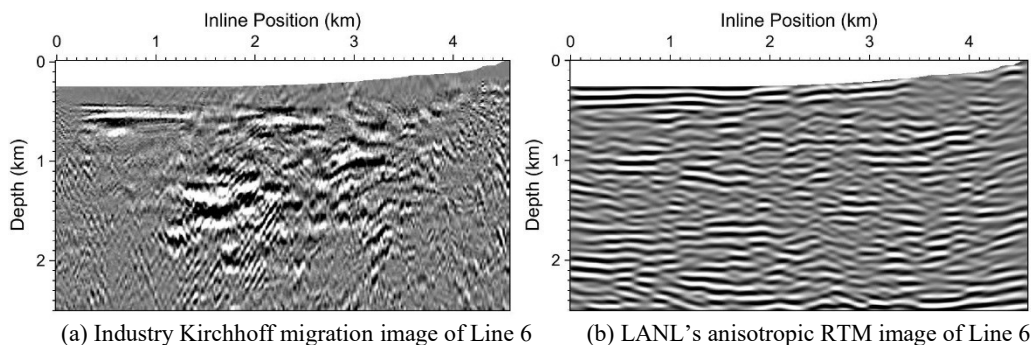
(a) Industry Kirchhoff migration image of Line 6

(b) LANL's anisotropic RTM image of Line 6

Figure 13: Line 6 image comparison between industry Kirchhoff migration image (a) and LANL's anisotropic reverse-time migration image (b).
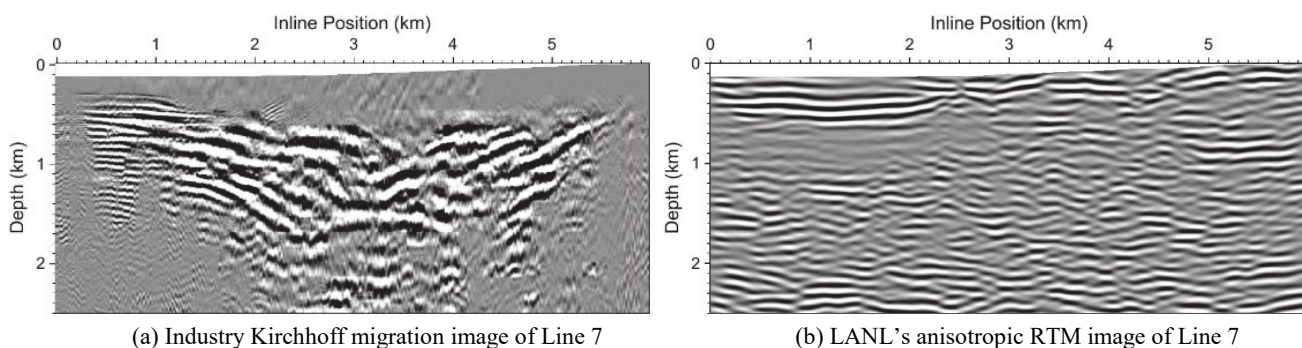

(a) Industry Kirchhoff migration image of Line 7

(b) LANL's anisotropic RTM image of Line 7

Figure 14: Line 7 image comparison between industry Kirchhoff migration image (a) and LANL's anisotropic reverse-time migration image (b).

(a) Industry Kirchhoff migration image
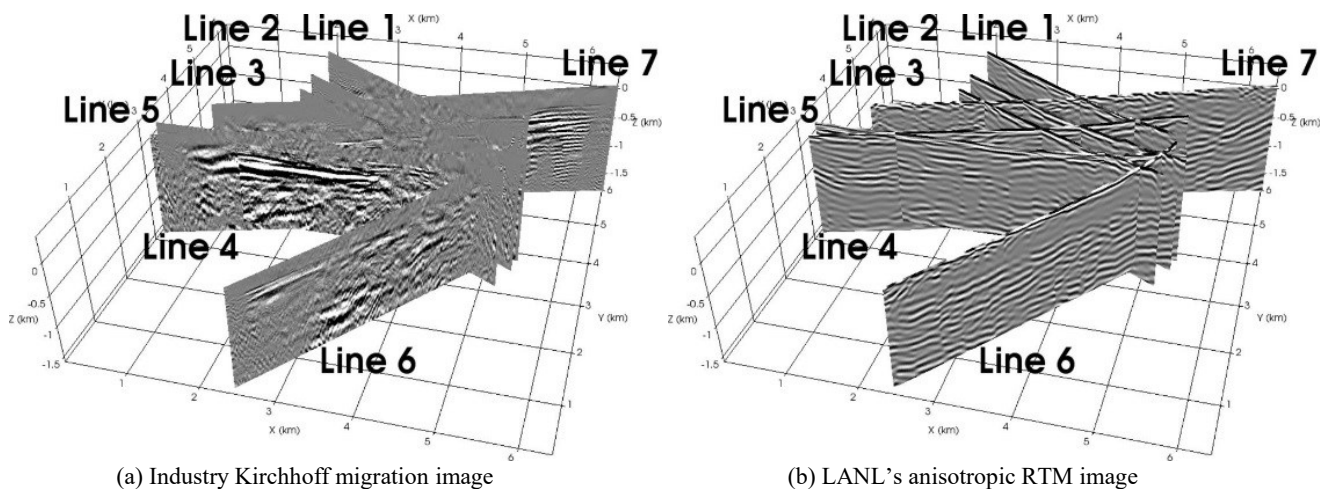
(b) LANL's anisotropic RTM image

Figure 15: Comparison between industry Kirchhoff migration images and LANL's anisotropic reverse-time migration images for all seven 2D lines of seismic data from the Blue Mountain geothermal field.

Figure 15 is a comparison between industry Kirchhoff migration images and LANL's anisotropic reverse-time migration images for all seven 2D lines of seismic data from the Blue Mountain geothermal field. It clearly shows the much improved image quality of our anisotropic reverse-time migration images compared to that of Kirchhoff migration images.

9

Huang et al.

4. CONCLUSIONS

We have successfully reduced strong ground-roll noise in 2D seismic data acquired along seven seismic survey lines at the Blue Mountain geothermal field, obtained anisotropic elastic parameters using our novel anisotropic elastic-waveform inversion, and produced high-quality migration images using our anisotropic reverse-time migration. Our new migration images contain significantly less noise than those generated using industry Kirchhoff migration, and clearly image a lot of subsurface reflectors that are invisible on the Kirchhoff migration images. Our high-quality, high-resolution migration images could help inform future decisions about which wells to hydraulically stimulate and where to site potential new injectors or producers.

5. ACKNOWLEDGEMENTS

REFERENCES

AltaRock Energy, Inc.: Blue Mountain Resource Review (2013).

Chen, T., and Huang, L.: Directly imaging steeply-dipping fault zones in geothermal fields with multicomponent seismic data, *Geothermics*, **57**, (2015), 238-245.

Chi, B., Dong, L., and Liu, Y.: Correlation-based reflection full-waveform inversion. *Geophysics*, **80**, (2015), R189-R202.

Chi, B., Gao, K., Huang, L.: Least-squares reverse time migration guided full-waveform inversion, *SEG Technical Program Expanded Abstracts*, 1471-1475, Houston, TX (2017).

Fei, T., Luo, Y., Yang, J., Liu, H. and Qin, F.: Removing false images in reverse time migration: The concept of de-primary: *Geophysics*, **80**, (2015), S237–S244.

Gao, K., Chi, B., and Huang, L.: Elastic least-squares reverse time migration with implicit wavefield separation, *SEG Technical Program Expanded Abstracts*, 4389-4394, Houston, TX (2017).

Chang, W.-F., and McMechan, G.A.: Reverse-time migration of offset vertical seismic profiling data using the excitation-time imaging condition, *Geophysics*, **51**, (1986), 67-84.

Chang, W.-F., and McMechan, G.A.: Elastic reverse-time migration, *Geophysics*, **52**, (1987), 1365-1375.

Gray, S.H., and May, W.P.: Kirchhoff migration using eikonal equation traveltimes. *Geophysics*, **59,** (1994), 810-817.

Huang, Y., Zhang, M., and Huang, L.: Ground-roll noise suppression in land surface seismic data using a wavenumber-adaptive bandpass filter, *Geothermal Resources Council Transactions*, **41**, (2017), 1659–1668.

Keho, T. H., and Beydoun, W. B.: Paraxial ray Kirchhoff migration." *Geophysics*, **53**, (1988), 1540-1546.

Lin, Y., and Huang, L.: Acoustic-and elastic-waveform inversion using a modified total-variation regularization scheme, *Geophysical Journal International*, **200**, (2014), 489-502.

Lin, Y., and Huang, L.: Building subsurface velocity models with sharp interfaces using interface-guided seismic full-waveform inversion, *Pure and Applied Geophysics*, **174**, (2017), 4035–4055.

Optim Software and Data Solutions: Final Technical Report: Active Source Seismic Exploration and Development at the Blue Mountain Geothermal Project, Humboldt County, Nevada (2007).

Swyer, M., Uddenberg, M., Nordin, Y., Cladouhos, T., and Petty, S.: Improved Injection Strategies at Blue Mountain, Nevada Through an Improved Conceptual Model, Tracer Testing, and Injection-production Correlation, *Proceedings*: 41st Workshop on Geothermal Reservoir Engineering, Stanford, CA (2016).

Tan, S., and Huang, L.: Least-squares reverse-time migration with a wavefield-separation imaging condition and updated source wavefields, *Geophysics*, **79**, (2014), S195-S205.

Tarantola, A.: Inversion of seismic reflection data in the acoustic approximation, *Geophysics*, 49, (1984), 1259–1266.

Thomsen, L.: Weak elastic anisotropy, *Geophysics*, **51**, (1986), 1954-1966.

Vigh D., Jiao, K., Watts, D., and Sun, D.: Elastic full-waveform inversion application using multicomponent measurements of seismic data collection: *Geophysics*, **79**, (2014), R63-R77.